A Direct Material Reconstruction Method for DECT Based on Total Variation and BM3D Frame

WENKUN ZHANG, AILONG CAI, ZHIZHONG ZHENG, LINYUAN WANG, NINGNING LIANG, LEI LI, BIN YAN, AND GUOEN HU
Department of Information System Engineering, Information Engineering University, Zhengzhou 450002, China

Corresponding author: Bin Yan (ybspace@hotmail.com)

ABSTRACT Dual-energy computed tomography (DECT) has attracted the attention of clinical researchers because of its outstanding capabilities to identify and decompose materials. Considering that material decomposition is unstable, reconstructed material images experience severe noise magnification resulting from the measurement data. To alleviate this problem, we propose a direct material reconstruction method by establishing a novel constrained reconstruction model based on total variation (TV) and block matching 3D (BM3D) frame regularization. TV regularization preserves the sparsity in the gradient domain of material maps and helps to preserve the image edges. BM3D frame is applied to depict the similarities among various patches in reconstructed images by grouping similar 2D image blocks into 3D data arrays combined with sparse transforms. To solve the program efficiently, a practical algorithm based on alternating direction method is developed. A modified strategy of block matching denoising is designed by incorporating the polychromatic reconstructed image into the problem solution. Digital and real data phantom studies are performed to validate the performance of the proposed method. The proposed method reduces the standard deviation on the selected region of interests by an average of 95.02% and 89.03% for the digital phantom and 95.21% and 84.19% for the real data compared with the extended simultaneous algebraic reconstruction technique and TV-based method, respectively. The reconstruction results demonstrate that the proposed method has promising capabilities in direct material reconstruction and superiority over its counterparts.

INDEX TERMS Dual-energy CT, direct material reconstruction BM3D frame, total variation.

I. INTRODUCTION

Dual-energy computed tomography (DECT) has attracted the attention of clinical researchers in recent years [1]–[3]. Comparing to the conventional CT which only uses one x-ray spectrum, DECT scans objects with high- and low-energy x-ray spectra, which enables it to characterize different tissues [4], [5]. Dual-energy measurement data can be collected by the advanced DECT imaging systems [6] such as dual-source, dual-detector, and fast kVp switching CT systems. With the development of hardware and techniques, DECT has been widely used in medical imaging [7], [8]

Three types of methods, i.e., projection domain-based, image domain-based, and direct reconstruction methods, are always used to reconstruct basis materials from dual-energy measurement data [9]. For the projection domain-based

method [10], [11], the independent sinograms of the basis materials are initially decomposed from dual-energy projections, and then material maps are reconstructed by the conventional filtered backprojection (FBP) method [12]. This method can achieve good reconstruction results in theory, but it requires geometrically consistent projections, which is a challenge for some DECT systems, such as dual-source [13] and fast kVp switching CTs [14]. For the image domain-based method [15], [16], high- and low-energy CT images are initially reconstructed from dual-energy spectra measurements, and then material decomposition is performed on dual-energy CT images. This method does not require the geometry consistency of dual-energy projections, but it fails to elaborate the nonlinear relationship between the polychromatic projections and basic materials. Comparing to the former two methods, the direct reconstruction method allows accurately modeling the DECT imaging and can directly reconstruct basis material maps from dual-energy

The associate editor coordinating the review of this manuscript and approving it for publication was Hengyong Yu.

projections [17], [18]. The direct reconstruction method (also called one-step method) can accommodate different CT scanners. However, the computational complexity to get the solution of the model makes the decomposition process unstable and the decomposition results are sensitive to image noises [19], leading to the decline of image quality on the reconstructed material maps.

Various regularization-based methods have been developed to optimize the solution of direct reconstruction model [20]. Total variation (TV) regularization-based methods have demonstrated their success in conventional CT [21]–[23] and other restoration issues such as phase retrieval [24]. Inspired by the potential performance of TV in noise suppression, Barber et al. developed a direct reconstruction algorithm for TV-constrained data discrepancy minimization and employed the constrained direct reconstruction algorithm for spectral CT data [25]. On this basis, Chen et al. designed a nonconvex optimization program incorporated with TV regularization term to reconstruct images directly from dual-energy data [26]. This direct reconstruction method can effectively compensate the nonlinear spectral response of DECT. However, for DECT, TV regularization-based methods encounter the same challenges as conventional CT in which oversmoothing and staircase effects are observed on the final results due to their assumption that the image is piecewise constant [27], [28]. To alleviate this problem, low-rank regularization is used to determine the correlation of interchannel images [29], [30]. Chu et al. combined low-rank and TV regularizations with a Split Bregman method for multienergy CT reconstruction [31]. Kim et al. used a patch-based low-rank penalty on reconstructed images for sparse view reconstruction in spectral CT [32]. Zhang et al. developed a tensor-based dictionary learning (TDL) method with the assumption of low-rank characteristic along the spectral dimension [33]. To overcome the weakness of TDL on preserving edge information, Wu et al. then emphasized the spatial sparsity by proposing an improved TDL method with a constraint of image gradient L0-norm [34] and obtained improved reconstruction performance in low-dose spectral CT. In the aforementioned studies, multichannel CT images are necessary for low-rank regularization-based methods. However, material reconstruction in DECT is performed on only two channels of CT images (high- and low-energy spectra CT images) and the correlation of interchannel images cannot be sufficiently explored through low-rank regularization.

Recently, similarities have been observed among various patches in medical images [35]–[37]. A direct method of utilizing these similarities is to express the images by grouping similar 2D image blocks into 3D data arrays combined with sparse transforms. The frame of block matching 3D (BM3D) was initially proposed for natural image denoising [38] and then this frame was extended to image deblurring and inpainting [39]. BM3D frame consists of two steps. The first step generates a basic estimate of the denoised image through a hard threshold filtration. In the second step the basic estimate

is used as the pilot signal for the index set of similar image blocks and empirical parameters to generate the final estimate of denoised image. The basic estimate with high quality in the first step helps to generate the final estimated image with low noise level. In 2017, Harrison et al. introduced the BM3D frame into spectral CT [40] in which a multichannel block matching denoising algorithm was proposed by utilizing the correlation and alignment between energy bins. In 2018, Wu et al. incorporated the BM3D frame into the material reconstruction of spectral CT and demonstrated that block matching regularization outperformed other nonlocal means [19]. Morteza et al. initially reconstructed a material image by using a low-rank regularization model and then performed block matching denoising on the decomposed results of spectral CT [41]. Shi et al. incorporated BM3D into an constrained phase retrieval framework as a regularization term [42] and then modified it as a plug-and-play form to recover an image from non-linear measured data [43], leading the improvement of imaging results. Inspired by the promising performance of BM3D frame on image denoising, we incorporate the BM3D frame into the TV-regularization reconstruction model of DECT to explore and utilize the similarities among the image patches of basis materials.

We propose a direct reconstruction method based on TV and BM3D frame for the direct material reconstruction of DECT. TV regularization term can preserve the sparsity in gradient domain of material images and can maintain the edge information BM3D frame can provide a promising depiction for the similarity of image patches. A novel reconstruction model of DECT is established by simultaneously incorporating the TV and BM3D frame as regularization terms. Alternating direction method is used to solve the optimization problem by splitting it into three sub-problems. One thing should be noted that when we perform the block matching-based denoising the material image is replaced by the polychromatic CT image as the prior image in the first step to generate the pilot image for the final estimate. Experiments on digital and real data phantoms validate the performance of the proposed method in direct material reconstruction of DECT. The paper is organized as follows. Sec II presents the proposed methodology and Sec III illustrates the experiment evaluation. The explanation of the experimental results of digital and real data is described in Sec IV Sec. V provides the discussion and conclusion of this study

II. METHODOLOGY
A. RECONSTRUCTION MODEL BASED ON TV AND BM3D FRAME
In DECT imaging, we consider the two-basis decomposition case and the discrete projection model for spectrum S can be represented as follows:

$$\mathbf{p}_j(\mathbf{b}_1, \mathbf{b}_2)$$
$$= -\ln \sum_m S_{j_m} \exp\left(-A\left(\mu_{1m}\mathbf{b}_1 + \mu_{2m}\mathbf{b}_2\right)\right), \quad j = H, L, \quad (1)$$

where j represents the spectrum index for low ($j = L$) and high ($j = H$) energy spectra, S_{j_m} is the normalized x-ray spectrum at energy m for j energy spectra and satisfies $\sum_m S_{j_m} = 1$ and $\mathbf{p}_j(\mathbf{b}_1, \mathbf{b}_2)$ denotes the projection data at j energy spectra for the two basis material images $\mathbf{b}_1$ and $\mathbf{b}_2 \mu_{1m}$ and μ_{2m} is the linear attenuation coefficients of materials 1 and 2 in mm^{-1} at energy m, respectively. A represents the system matrix in $R^{M \times N}$ where N represents the total number of material pixels and M is the number of total x-ray paths. A is a forward projection operator calculated via the intersection length between x-rays and image pixels. The data model of Eq. (1) is a nonlinear function of basis materials $\mathbf{b}_1$ and $\mathbf{b}_2$. Let $\mathcal{A}_j$ represent the nonlinear operator of polychromatic projection and Eq. (1) can be rewritten as

$$\mathbf{p}_j = \mathcal{A}_j(\mathbf{b}_1, \mathbf{b}_2), \quad j = H, L \qquad (2)$$

In this study, we aim to explore the local and nonlocal sparsity characteristics of material image on the basis of TV and BM3D frame to generate a stable solution with low noise level. Similar to the optimization framework of other regularization-based iterative algorithms, the proposed method is formulated as the following constrained minimization problem:

$$\min_{\mathbf{b}_i, \mathbf{v}_i} \sum_{i=1,2} (\|\mathbf{v}_i\|_1 + \|\Phi(\mathbf{b}_i)\|_0)$$
$$s.t \; \nabla \mathbf{b}_i = \mathbf{v}_i, \quad i = 1, 2$$
$$\mathbf{p}_j = \mathcal{A}_j(\mathbf{b}_1, \mathbf{b}_2), \quad j = H, L \qquad (3)$$

where ∇ denotes the discrete directional gradient operators. The summation of horizontal and vertical operators which can be simply represented by ∇ are calculated in this work. Subscript i represents the index of basis material and j is the index of high- or low-energy spectra in DECT Since we focus on the case of two basis materials in this work, we can define that $i = 1, 2$. $\|\cdot\|_0$ denotes the -norm (it is a semi-norm) and Φ represents the operator of BM3D analysis operation [39], which includes block matching and discrete cosine transform (DCT).

B. SOLVING MODEL BASED ON THE ALTERNATING DIRECTION METHOD

For Eq (3), an efficient class of methods seeks for the minimizer by approaching the original constrained problem with a sequence of unconstrained sub-problems. An iterative solver is constantly considered in the design of the practical algorithm. In our work, considering the number of the unsolved variables and the nonlinearities of the optimization problem, we apply an augmented Lagrange function to convert the above constrained problem into an unconstrained form. In the procedure of iterative solution, since the iteration solution at one spectra is independent to another spectra, the high- and low-energy measurement projections are alternatively used to update the variables Thus Eq. (3) can be rewritten as two

problems corresponding to the high- and low-energy spectra:

$$L_{AH} = \min_{\mathbf{b}_i, \mathbf{v}_i} \sum_{i=1,2} \Big(\|\mathbf{v}_i\|_1 + \|\Phi(\mathbf{b}_i)\|_0 + \boldsymbol{\rho}_i^T$$
$$\times (\mathbf{v}_i - \nabla \mathbf{b}_i) + \frac{\beta}{2} \|\mathbf{v}_i - \nabla \mathbf{b}_i\|_2^2 \Big)$$
$$+ \boldsymbol{\lambda}_H^T (\mathcal{A}_H(\mathbf{b}_1, \mathbf{b}_2) - \mathbf{p}_H) + \frac{\theta}{2} \|\mathcal{A}_H(\mathbf{b}_1, \mathbf{b}_2) - \mathbf{p}_H\|_2^2, \quad (4)$$

$$L_{AL} = \min_{\mathbf{b}_i, \mathbf{v}_i} \sum_{i=1,2} \Big(\|\mathbf{v}_i\|_1 + \|\Phi(\mathbf{b}_i)\|_0 + \boldsymbol{\rho}_i^T$$
$$\times (\mathbf{v}_i - \nabla \mathbf{b}_i) + \frac{\beta}{2} \|\mathbf{v}_i - \nabla \mathbf{b}_i\|_2^2 \Big)$$
$$+ \boldsymbol{\lambda}_L^T (\mathcal{A}_L(\mathbf{b}_1, \mathbf{b}_2) - \mathbf{p}_L) + \frac{\theta}{2} \|\mathcal{A}_L(\mathbf{b}_1, \mathbf{b}_2) - \mathbf{p}_L\|_2^2. \quad (5)$$

where $\boldsymbol{\rho}_i$ and $\boldsymbol{\lambda}_j$ are the Lagrange multipliers and β and θ are the penalty coefficients. Eq. (4) and Eq. (5) can be solved in the same way in DECT Thus we take one spectra $j = H, L$ as an example to derive the complete process of model solution, which is written as

$$L_A = \min_{\mathbf{b}_i, \mathbf{v}_i} \sum_{i=1,2} \Big(\|\mathbf{v}_i\|_1 + \|\Phi(\mathbf{b}_i)\|_0 + \boldsymbol{\rho}_i^T$$
$$\times (\mathbf{v}_i - \nabla \mathbf{b}_i) + \frac{\beta}{2} \|\mathbf{v}_i - \nabla \mathbf{b}_i\|_2^2 \Big)$$
$$+ \boldsymbol{\lambda}_j^T (\mathcal{A}_j(\mathbf{b}_1, \mathbf{b}_2) - \mathbf{p}_j) + \frac{\theta}{2} \|\mathcal{A}_j(\mathbf{b}_1, \mathbf{b}_2) - \mathbf{p}_j\|_2^2. \quad (6)$$

Then, the unconstrained optimization problem of Eq. (6) can be divided into two sub-problems, $L_A(\mathbf{v}_i)$ and $L_A(\mathbf{b}_i)$

The first sub-problem $L_A(\mathbf{v}_i)$ can be written as follows with fixed $\mathbf{b}_i^k, \boldsymbol{\rho}_i^k$:

$$L_A(\mathbf{v}_i) = \min_{\mathbf{v}_i} \Big(\|\mathbf{v}_i\|_1 + \big(\boldsymbol{\rho}_i^k\big)^T \big(\mathbf{v}_i - \nabla \mathbf{b}_i^k\big) + \frac{\beta}{2} \big\|\mathbf{v}_i - \nabla \mathbf{b}_i^k\big\|_2^2 \Big),$$
$$i = 1, 2, \qquad (7)$$

Eq. (7) can be efficiently solved using a shrinkage operator and the solution of sub-problem $L_A(\mathbf{v}_i)$ in the $k+1$th iteration can be computed by

$$\mathbf{v}_i^{k+1} = \max \left(\left| \nabla \mathbf{b}_i^k - \frac{\boldsymbol{\rho}_i^k}{\beta} \right| - \frac{1}{\beta}, 0 \right)$$
$$\cdot sgn \left(\nabla \mathbf{b}_i^k - \frac{\boldsymbol{\rho}_i^k}{\beta} \right), \quad i = 1, 2. \quad (8)$$

where operator $sgn(\cdot)$ is an odd mathematical function that extracts the sign of a real number.

The second sub-problem $L_A(\mathbf{b}_i)$ can be written as follows with fixed $\mathbf{v}_i^{k+1}, \boldsymbol{\rho}_i^k, \boldsymbol{\lambda}_{ij}^k$:

$$L_A(\mathbf{b}_i) = \min_{\mathbf{b}_i} \Big(\|\Phi(\mathbf{b}_i)\|_0 + \big(\boldsymbol{\rho}_i^k\big)^T \big(\mathbf{v}_i^{k+1} - \nabla \mathbf{b}_i\big)$$
$$+ \frac{\beta}{2} \big\|\mathbf{v}_i^{k+1} - \nabla \mathbf{b}_i\big\|_2^2 \big(\boldsymbol{\lambda}_{ij}^k\big)^T (\mathcal{A}_j(\mathbf{b}_1, \mathbf{b}_2) - \mathbf{p}_j)$$
$$+ \frac{\theta}{2} \|\mathcal{A}_j(\mathbf{b}_1, \mathbf{b}_2) - \mathbf{p}_j\|_2^2 \Big), \quad i = 1, 2. \quad (9)$$

Directly solving the above sub-problem is a challenging work. Method in [19] solved this problem by introducing an auxiliary variable. Inspired by this idea, we continually separate the variables in Eq. (9) by introducing $\mathbf{g}_i = \mathbf{b}_i$. Then, the initial sub-problem can be written as constrained optimization problem:

$$\min_{\mathbf{b}_i, \mathbf{g}_i} \left(\|\Phi(\mathbf{b}_i)\|_0 + \Upsilon(\mathbf{g}_i) \right), \quad i = 1, 2,$$
$$s.t. \ \mathbf{g}_i = \mathbf{b}_i, \tag{10}$$

where Υ represents the operator of the initial sub-problem exclude the term of $\|\Phi(\mathbf{b}_i)\|_0$. Augmented Lagrange function is applied to convert Eq. (3) into an unconstrained form:

$$\min_{\mathbf{b}_i, \mathbf{g}_i} \left(\|\Phi(\mathbf{b}_i)\|_0 + \Upsilon(\mathbf{g}_i) + \frac{\sigma}{2} \left\| \mathbf{g}_i - \mathbf{b}_i + \frac{\boldsymbol{\gamma}_i}{\sigma} \right\|_G^2 \right), \quad i = 1, 2. \tag{11}$$

where $\boldsymbol{\gamma}_i$ and σ is the Lagrange multiplier and penalty parameter, respectively. $\|\|_G$ represents the elliptic norm and $G = \Phi^T \Phi$ is a diagonal matrix. Φ^T is the transposition of the matrix representation of BM3D analysis operation. (The detailed definition and relative proof of G can be found in [39]) Then, sub-problem $L_A(\mathbf{b}_i)$ can be split into two new sub-problems:

$$L_{A,sub}(\mathbf{g}_i)$$
$$= \min_{\mathbf{g}_i} \left(\Upsilon(\mathbf{g}_i) + \frac{\sigma}{2} \left\| \mathbf{g}_i - \mathbf{b}_i + \frac{\boldsymbol{\gamma}_i}{\sigma} \right\|_G^2 \right)$$
$$= \min_{\mathbf{g}_i} \left(\left(\boldsymbol{\rho}_i^k \right)^T \left(\mathbf{v}_i^{k+1} - \nabla \mathbf{g}_i \right) + \frac{\beta}{2} \left\| \mathbf{v}_i^{k+1} - \nabla \mathbf{g}_i \right\|_2^2 \right.$$
$$+ \left(\boldsymbol{\lambda}_{ij}^k \right)^T \left(\mathcal{A}_j(\mathbf{g}_1, \mathbf{g}_2) - \mathbf{p}_j \right) + \frac{\theta}{2} \left\| \mathcal{A}_j(\mathbf{g}_1, \mathbf{g}_2) - \mathbf{p}_j \right\|_2^2$$
$$+ \left. \frac{\sigma}{2} \left\| \mathbf{g}_i - \mathbf{b}_i + \frac{\boldsymbol{\gamma}_i}{\sigma} \right\|_G^2 \right), \quad i = 1, 2 \tag{12}$$

$$L_{A,sub}(\mathbf{b}_i)$$
$$= \min_{\mathbf{b}_i} \left(\|\Phi(\mathbf{b}_i)\|_0 + \frac{\sigma}{2} \left\| \mathbf{g}_i - \mathbf{b}_i + \frac{\boldsymbol{\gamma}_i}{\sigma} \right\|_G^2 \right), \quad i = 1, 2, \tag{13}$$

In our work, we aim to solve the above sub-problems to directly reconstruct material maps from the dual-energy measurement projections.

C. SOLVING THE NONLINEAR SUB-PROBLEM
One difficulty that should be considered in the solution of sub-problem $L_{A,sub}(\mathbf{g}_i)$ is that the nonlinear operator of $\mathcal{A}_j$ caused by the summation of Eq. (1) is located inside the logarithm operation. Inspired by the extended algebraic reconstruction technique [44], we unfold the data model of Eq. (1) with the first-order Taylor expansion at current point $(\mathbf{b}_1^k, \mathbf{b}_2^k)$ to the linear operator of $\mathcal{A}_j$. Let $\mathcal{F}_j$ denote the linearization of nonlinear operator $\mathcal{A}_j$ via the first-order Taylor operation. We can obtain the approximated expression of projection difference of basis materials, represented by $\tilde{\mathcal{P}}_{1j}^k$ and $\tilde{\mathcal{P}}_{2j}^k$ in our work, at the representation of linear operator A [45]. The detailed derivation can be found in the Appendix.

The sub-problem $L_{A,sub}(\mathbf{g}_i)$ based on the linearization of the data model with fixed $\mathbf{v}_i^{k+1}, \mathbf{b}_i^k, \boldsymbol{\rho}_i^k, \boldsymbol{\gamma}_i^k, \boldsymbol{\lambda}_{ij}^k$ can be rewritten as

$$L_{A,sub}(\mathbf{g}_i)$$
$$= \min_{\mathbf{g}_i} \left(\left(\boldsymbol{\rho}_i^k \right)^T \left(\mathbf{v}_i^{k+1} - \nabla \mathbf{g}_i \right) + \frac{\beta}{2} \left\| \mathbf{v}_i^{k+1} - \nabla \mathbf{g}_i \right\|_2^2 \right.$$
$$+ \left(\boldsymbol{\lambda}_{ij}^k \right)^T \left(\mathcal{F}_j \mathbf{g}_i - \mathbf{p}_j \right) + \frac{\theta}{2} \left\| \mathcal{F}_j \mathbf{g}_i - \mathbf{p}_j \right\|_2^2$$
$$+ \left. \frac{\sigma}{2} \left\| \mathbf{g}_i - \mathbf{b}_i^k + \boldsymbol{\gamma}_i^k/\sigma \right\|_G^2 \right), \quad i = 1, 2. \tag{14}$$

To reduce the computational costs of pseudo inverse, we adopt an inexact alternative direction method (ADM) that utilizes linearization and proximal points [46]. This method can linearize fidelity terms at current point $\mathbf{g}_i^k$ and add proximal terms. In mathematical expression, the elliptic norm of $\mathbf{x} = \mathbf{g}_i - \mathbf{b}_i^k + \boldsymbol{\gamma}_i^k/\sigma$ can be calculated by $\|\mathbf{x}\|_G^2 = \mathbf{x}^T G \mathbf{x}$ and we obtain $\mathbf{x}^T G \mathbf{x} = \mathbf{x}^T \Phi^T \Phi \mathbf{x} = \|\Phi(\mathbf{x})\|_2^2$. Thus, the quadratic terms of Eq. (14) can be rewritten as:

$$\left\| \mathcal{F}_j \mathbf{g}_i - \mathbf{p}_j \right\|_2^2$$
$$\approx \left\| \mathcal{F}_j \mathbf{g}_i^k - \mathbf{p}_j \right\|_2^2 + 2\mathbf{h}_{ij}^T \left(\mathbf{g}_i - \mathbf{g}_i^k \right) + \frac{1}{\tau} \left\| \mathbf{g}_i - \mathbf{g}_i^k \right\|_2^2 \tag{15}$$

$$\left\| \Phi \left(\mathbf{g}_i - \mathbf{b}_i^k + \boldsymbol{\gamma}_i^k \sigma \right) \right\|_2^2$$
$$\approx \left\| \Phi \left(\mathbf{g}_i^k - \mathbf{b}_i^k + \boldsymbol{\gamma}_i^k/\sigma \right) \right\|_2^2 + 2\mathbf{r}_i^T \left(\mathbf{g}_i - \mathbf{g}_i^k \right) + \frac{1}{\tau'} \left\| \mathbf{g}_i - \mathbf{g}_i^k \right\|_2^2 \tag{16}$$

where $\mathbf{h}_{ij} = \mathcal{F}_j^T \left(F_j \mathbf{g}_i^k - \mathbf{p}_j \right) \mathbf{r}_i = \Phi^T \Phi \left(\mathbf{g}_i^k - \mathbf{b}_i^k + \boldsymbol{\gamma}_i^k/\sigma \right)$. Then Eq. (14) can be written as follows:

$$\min_{\mathbf{g}_i} \left(\left(\boldsymbol{\rho}_i^k \right)^T \left(\mathbf{v}_i^{k+1} - \nabla \mathbf{g}_i \right) + \frac{\beta}{2} \left\| \mathbf{v}_i^{k+1} - \nabla \mathbf{g}_i \right\|_2^2 \right.$$
$$+ \left(\boldsymbol{\lambda}_{ij}^k \right)^T \left(\mathcal{F}_j \mathbf{g}_i - \mathbf{p}_j \right) + \frac{\theta}{2} \left\| \mathcal{F}_j \mathbf{g}_i^k - \mathbf{p}_j \right\|_2^2 + \theta \mathbf{h}_{ij}^T \left(\mathbf{g}_i - \mathbf{g}_i^k \right)$$
$$+ \frac{\theta}{2\tau} \left\| \mathbf{g}_i - \mathbf{g}_i^k \right\|_2^2 + \frac{\sigma}{2} \left\| \Phi \left(\mathbf{g}_i^k - \mathbf{b}_i^k + \boldsymbol{\gamma}_i^k/\sigma \right) \right\|_2^2$$
$$+ \left. \sigma \mathbf{r}_i^T \left(\mathbf{g}_i - \mathbf{g}_i^k \right) + \frac{\sigma}{2\tau'} \left\| \mathbf{g}_i - \mathbf{g}_i^k \right\|_2^2 \right), \quad i = 1, 2. \tag{17}$$

Let the derivative of Eq. (17) with respect to $\mathbf{g}_i$ and force the results to be zero, we obtain the following:

$$\mathbf{g}_i^{k+1} = \left(\beta \nabla^T \nabla + \left(\frac{\theta}{\tau} + \frac{\sigma}{\tau'} \right) I \right)^+ \left(\nabla^T \boldsymbol{\rho}_i^k + \beta \nabla^T \mathbf{v}_i^{k+1} \right.$$
$$- \mathcal{F}_j^T \boldsymbol{\lambda}_{ij}^k - \theta \mathbf{h}_{ij} + \frac{\theta}{\tau} \mathbf{g}_i^k - \sigma \mathbf{r}_i + \frac{\sigma}{\tau'} \mathbf{g}_i^k \left. \right), \quad i = 1, 2. \tag{18}$$

Matrix $\left(\beta \nabla^T \nabla + \left(\frac{\theta}{\tau} + \frac{\sigma}{\tau'} \right) I \right)$ can be diagonalized through fast Fourier transform [47], which can simultaneously accelerate iterations and maintain accuracy. Let $M = \mathbb{F} \left(\beta \nabla^T \nabla + \left(\frac{\theta}{\tau} + \frac{\sigma}{\tau'} \right) I \right) \mathbb{F}^{-1}$ and the solution of Eq. (18) can

be obtained by

$$\mathbf{g}_i^{k+1} = \mathbb{F}^{-1} \left(M^{-1} \mathbb{F} \left(\nabla^T \boldsymbol{\rho}_i^k + \beta \nabla^T \mathbf{v}_i^{k+1} - \mathcal{F}_j^T \boldsymbol{\lambda}_{ij}^k \right. \right.$$
$$\left. \left. -\theta \mathbf{h}_{ij} - \frac{\theta}{\tau} \mathbf{g}_i^k - \sigma \mathbf{r}_i + \frac{\sigma}{\tau'} \mathbf{g}_i^k \right) \right), \quad i = 1, 2. \quad (19)$$

The residual term in $\mathbf{h}_{ij} = \mathcal{F}_j^T \left(\mathcal{F}_j \mathbf{g}_i^k - \mathbf{p}_j \right)$ can be approximated by $\tilde{P}_i^k$, which takes the basis of the linear expression of projection operator A Thus Eq. (19) can be approximated as

$$\mathbf{g}_i^{k+1} = \mathbb{F}^{-1} \left(M^{-1} \mathbb{F} \left(\nabla^T \boldsymbol{\rho}_i^k + \beta \nabla^T \mathbf{v}_i^{k+1} - A^T \left(\boldsymbol{\lambda}_{ij}^k + \theta \tilde{\mathcal{P}}_{ij}^k \right) \right. \right.$$
$$\left. \left. + \frac{\theta}{\tau} \mathbf{g}_i^k - \sigma \mathbf{r}_i + \frac{\sigma}{\tau'} \mathbf{g}_i^k \right) \right), \quad i = 1, 2. \quad (20)$$

### D. SOLVING THE SUB-PROBLEM OF BLOCK MATCHING

For the sub-problem $L_{A,\text{sub}}(\mathbf{b}_i)$, we update $\mathbf{b}_i$ with respect to fixed $\mathbf{g}_i^{k+1}$. A hard thresholding method can be used to solve $L_{A,\text{sub}}(\mathbf{b}_i)$ with the L_0-norm of 3D transform domain coefficients. Then, the update of $\mathbf{b}_i$ can be calculated by

$$\mathbf{b}_i^{k+1} = \Psi \left\lfloor \Phi \left(\mathbf{g}_i^{k+1} + \frac{\boldsymbol{\gamma}_i^k}{\sigma} \right) \right\rfloor_{\kappa_i}, \quad i = 1, 2, \quad (21)$$

where Ψ represents the inverse 3D sparse transform of operator Φ Operator $\lfloor \cdot \rfloor_{\kappa_i}$ represents the hard thresholding operation, which can be calculated by

$$\lfloor \Phi(\cdot) \rfloor_{\kappa_i} = \begin{cases} 0, & \Phi(\cdot) < \sqrt{\kappa_i}, \\ \Phi(\cdot), & \Phi(\cdot) \geq \sqrt{\kappa_i}. \end{cases} \quad (22)$$

Inspired by the idea in [19], this problem can be converted into the operation of BM3D denoising. At the basis of the BM3D method, we design a new image denoising strategy for the material reconstruction of DECT in this work. Considering that the coordinates of similar image blocks on the reconstructed CT image are almost consistent with the material maps, we substitute the initial denoised images, i.e., decomposed material maps, with a polychromatic CT image which is reconstructed from the collected projection via the FBP method as the input image in the first step In comparison with the material images, the reconstructed CT image has a low noise level, which can help improve the accuracy of block grouping and generate a high quality of basic estimate. As the decomposed material images are seriously blurred and anamorphic at the beginning of the iteration, utilizing the reconstructed CT image to generate the pilot image for the second step of BM3D is more promising than the initial decomposed material images. In our work, the low-energy CT image is used to generate the basic estimate because it has better gray contrast for different materials than the high-energy CT image (the selection of prior image is discussed in Section V). Fig. 1 shows the entire workflow of the modified denoising strategy The complete formulas including the operation of block matching, collaborative filtering, and block aggregation can be found in [38]. To streamline the derivation of the whole manuscript, we only illustrate
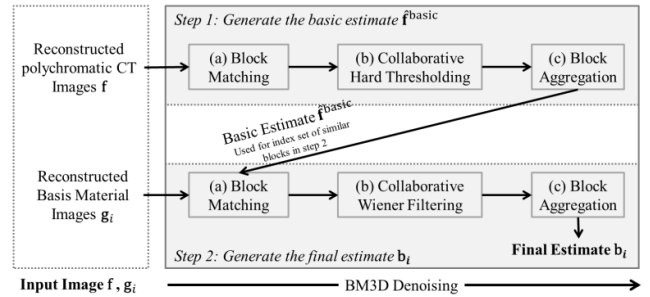
FIGURE 1. Workflow of the designed denoising method based on BM3D. The input images of BM3D denoising are the reconstructed polychromatic CT image f and basis material image g_i. In step 1, f is used to generate the basic estimate $\hat{f}^{\text{basic}}$ for the index set of similar blocks in step 2. In step 2, the basic estimate $\hat{f}^{\text{basic}}$ and basis material image g_i are used to generate the final estimate b_i.

the main difference between the proposed method and the conventional BM3D method.

As shown in Fig. 1, the entire workflow includes two steps. The reconstructed low-energy polychromatic CT image $\mathbf{f}$ is firstly inputted into the first step, and the basic estimate $\hat{\mathbf{f}}^{\text{basic}}$ can be generated after the block matching, collaborative hard thresholding, and block aggregation. We use the basic estimate $\hat{\mathbf{f}}^{\text{basic}}$ to calculate the block distance and generate the coordinates of similar blocks for the reconstructed basis material map $\mathbf{g}_i$. In the second step, let $\hat{F}_x^{\text{basic}}$ and $\hat{F}_{x_R}^{\text{basic}}$ represent the slide and reference blocks of $\hat{\mathbf{f}}^{\text{basic}}$ with the size of $N_1 \times N_1$, where x and x_R denotes their 2D spatial coordinate that belongs to image domain X. The distance and coordinate set of similar blocks can be calculated by

$$d\left(\hat{F}_{x_R}^{\text{basic}}, \hat{F}_x^{\text{basic}} \right) = \frac{\left\| \mathcal{T}_{2D} \left(\hat{F}_{x_R}^{\text{basic}} \right) - \mathcal{T}_{2D} \left(\hat{F}_x^{\text{basic}} \right) \right\|_2^2}{(N_1)^2} \quad (23)$$

$$S_{x_R}^{\text{wie}} = \left\{ x \in X : d\left(\hat{F}_{x_R}^{\text{basic}}, \hat{F}_x^{\text{basic}} \right) \leq \eta_{\text{match}}^{\text{wie}} \right\} \quad (24)$$

where $\mathcal{T}_{2D}$ denotes the normalized 2D linear transform, such as DCT, and $\eta_{\text{match}}^{\text{wie}}$ is the maximum distance of two similar blocks. On the basis of the coordinate set of similar patches $S_{X_R}^{\text{wie}}$, the block groups of noisy material maps $\mathbf{g}_i$ can be obtained as $\mathbf{G}_{S_{X_R}^{\text{wie}}}$ by grouping the similar image blocks Then, the collaborative wiener filtering and block aggregation are performed on the block groups $\mathbf{G}_{S_{X_R}^{\text{wie}}}$ to generate the final estimate of material image $\mathbf{b}_i^{k+1}$

E. METHOD WORKFLOW AND PARAMETER SELECTION

The proposed method includes the solution of three sub-problems. Three variables are first updated using the measurement projection data at low-energy spectra and then updated using the projection data at high-energy spectra. The scheme of the proposed method can be illustrated as follows:

In the above method, β, θ, and σ are the weights of the three regularization terms. They are determined in accordance with the sparsity feature of the underlying image and

1. Initialization $\beta, \theta, \sigma, \delta, k = 0, K$

2. $j = L$

3. Solving sub-problem 1:

$$\mathbf{v}_i^{k+1} = \max \left(\left\| \nabla \mathbf{b}_i^k - \frac{\boldsymbol{\rho}_i^k}{\beta} \right\|_1 - \frac{1}{\beta}, 0 \right)$$
$$\cdot sgn \left(\nabla \mathbf{b}_i^k - \frac{\boldsymbol{\rho}_i^k}{\beta} \right), \quad i = 1, 2$$

4. Solving sub-problem 2:

$$\mathbf{g}_i^{k+1}$$
$$= \mathbb{F}^{-1} \left(M^{-1} \cdot F \left(\nabla^T \boldsymbol{\rho}_i^k + \beta \nabla^T \mathbf{v}_i^{k+1} - A^T \left(\boldsymbol{\lambda}_{ij}^k + \theta \tilde{\mathcal{P}}_{ij}^k \right) \right. \right.$$
$$\left. \left. + \frac{\theta}{\tau} \mathbf{g}_i^k - \sigma \mathbf{r}_i + \frac{\sigma}{\tau'} \mathbf{g}_i^k \right) \right), \quad i = 1, 2$$

5. Solving sub-problem 3:

$$\mathbf{b}_i^{k+1} = \arg\min_{\mathbf{b}_i} \left(\left\| \Phi \left(\mathbf{b}_i^k \right) \right\|_0 + \frac{\sigma}{2} \left\| \mathbf{g}_i^{k+1} - \mathbf{b}_i^k + \frac{\boldsymbol{\gamma}_i^k}{\sigma} \right\|_G^2 \right),$$
$$i = 1, 2$$

6. Updating Lagrange multipliers:

$$\begin{cases} \boldsymbol{\rho}_i^{k+1} = \boldsymbol{\rho}_i^k + \beta \left(\mathbf{v}_i^{k+1} - \nabla \mathbf{b}_i^{k+1} \right) \\ \boldsymbol{\gamma}_i^{k+1} = \boldsymbol{\gamma}_i^k + \sigma \left(\mathbf{g}_i^{k+1} - \mathbf{b}_i^{k+1} \right) \quad i = 1, 2 \\ \boldsymbol{\lambda}_{ij}^{k+1} = \boldsymbol{\lambda}_{ij}^k - \theta \tilde{\mathcal{P}}_{ij}^k, \end{cases}$$

7. $j = H$ and updating variables on the basis of programs 3 to 6

8. End if the algorithm reaches maximal iteration K

noise level in the observation. β should be large when the underlying image contains high-level noises. θ has positive correlation with the speed of convergence, but it may decrease the effects of regularization and introduce noises when the measurement data contains large inconsistencies. For σ, it should be smaller than β and θ. A simple method to determine their values is by using different values from 2^3 up to 2^9 and comparing the decomposed material maps.

During block matching, parameter δ plays an important role in image denoising. The larger δ is, the stronger block matching filter has. In general, δ ranging from 0.2 to 5 is acceptable for most denoising tasks. According to our experience δ is set to 0.4 for the digital simulation and 1.5 for the real data in our work. Considering that block matching is included in the scheme of ADM, other parameters of block matching may show relatively small influence on the final results and their settings refer to the parameters of [48]. Image patch size N_1 is set to 8 for both filtering steps. Distance thresholds $\eta_{\text{match}}^{\text{wie}}$ are set 400. In the implementation of the
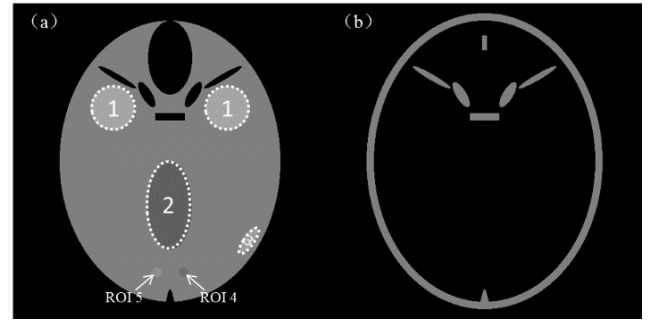

FIGURE 2. (a) Normalized tissue material map; (b) normalized bone material map. The display window of both figures is [0.8 1.2].

proposed method, variable $\mathbf{b}_i$ updates every five iterations to reduce the running time occupied by block matching denoising. The running time of each iteration will be discussed in Section V.

III. EVALUATION

The performance of the proposed method is tested using both digital phantom and real data. We compare the proposed method with the extended simultaneous algebraic reconstruction technique (ESART) [49] as well as its TV minimization algorithm, which minimizes the TV of the material maps by steepest descent The algorithm that solely utilizes BM3D is also provided by incorporating BM3D into the scheme of ESART method. Besides, we compare the difference of L1 and L norm of BM3D frame for the proposed method in the experiments. The parameters are the same for the proposed methods with L1 and L0 norm in our experiments. The proposed method with L1 norm combines the L1 norm of BM3D frame and TV regularization term, which is different with the TV-based method that solely contains the TV regularization term. Maximal iteration K is set to 100. The initial guess of all methods is generated based on the reconstructed low-energy CT image using a threshold segmentation method. The threshold is selected based on the attenuation coefficients of different material on the CT image. The image pixels whose gray values are greater than the threshold constitute the initial map of one material, the others consist of the initial map of another material. Value normalization is performed on two initial maps before they are inputted into the iteration of the direct reconstruction methods All of the experiments are performed on a HP Z820 workstation with Intel Xeon E5-2650 CPU 2.6 GHz and a Nvidia TITAN V GPU.

The digital phantom is constructed on the basis of the Forbild phantom with a size of 512×512 pixels. Fig. 2(a) shows the map of the tissue material with seven gray levels, including the background in which the value is zero. Fig. 2(b) presents the map of the pure bone material with one gray value. They are used to generate the high- and low-energy projections of the digital phantom. Fig. 3(a) displays the high- and low-energy spectra at the tube voltage of 140 and 80 kVp, which are generated by SpekCalc software. The energy
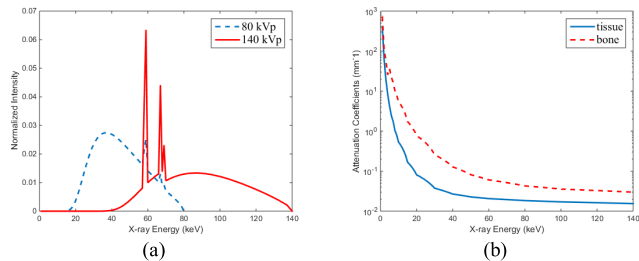
FIGURE 3. (a) High- (red solid line) and low-energy (blue dashed line) spectra with an energy increment interval of 1 keV. (b) Attenuation coefficients of bone (red dashed line) and tissue (blue solid line) materials at 140 kVp.

FIGURE 4. (a) QRM phantom used in real data experiments. (b) Illustration of five compositions of QRM phantom, i.e., cortical mandible bone, spongious bone, muscle, CT water, and adipose.

spectra is sampled with an interval of 10 keV in our experiment. Fig. 3(b) shows the attenuation coefficients of the bone and tissue, which are retrieved from the National Institute of Standards and Technology database. The source-to-object and source-to-detector distances is 500 and 1000 mm, respectively. Projection samples in each view are collected using a linear detector that consists of 1024 bins with a size of 0.35 mm × 0.35 mm. Dual-energy projections are acquired at 360° rotation with a scanning interval of 1°. Noises are added to dual-energy projections, which are generated by the Poisson model as follows:

$$N_{\mathbf{p}} = \text{Poisson}\left(N_{\mathbf{p}0} \exp\left(-\mathbf{p}\right)\right) \quad (25)$$

where $N_{\mathbf{p}0}$ is the number of incident x-ray photons and $\mathbf{p}$ represents the measured number of photons in the projection. $N_{\mathbf{p}0}$ is set as 1×10^5. The decomposed images have a dimension of 512×512 and the pixel size is 0.25 mm × 0.25 mm. We compare the decomposition results and their difference maps with the ground truth image for different methods. The recovered details of decomposition results can be evaluated by an enlarged region including two circle areas with low contrast. The line profiles of decomposition results are provided to compare the decomposition accuracy. To quantitatively evaluate the performance of all reconstruction methods, the root mean square error (RMSE), peak-signal-to-noise ratio (PSNR), and structural similarity (SSIM) are calculated on the decomposed maps of tissue and bone materials. In addition, the robustness of the proposed method can be evaluated by the mean values and noise standard derivation (STD) of five uniform regions of interest (ROIs) (as show in Fig. 2(a)), which is defined as

$$\text{STD} = \sqrt{\frac{1}{N_{\text{ROI}}} \sum_{l=1}^{N_{\text{ROI}}} (x_l - \bar{x})}, \quad (26)$$

where l is the pixel index of ROI and x_l represents the value of the lth pixel. $\bar{x}$ denotes the mean value of all N_{ROI} image pixels belonging to the objective ROI. We also use the curves of RMSE and the curves of the L1 norm of image gradients to compare the convergence of different methods. Furthermore, the pseudo-monochromatic CT images at 60 keV are provided by linearly forming the material maps of digital phantom to evaluate the material reconstruction quality.
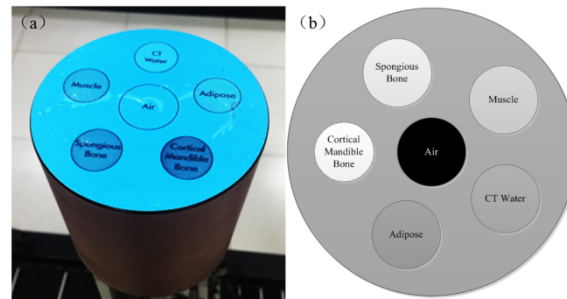
The experiments on real data are performed using an industrial CT system in our laboratory. The cone-beam CT system is mainly composed of an x-ray source (Hawkeye 130, Thales, France), orthogonally rotary stage with object holder, and flat panel detector (4030E, Varian, USA). We use an QRM phantom to perform the experiments on real data (Fig. 4(a)). As shown in Fig. 4(b), the QRM phantom has five different tissue equivalent materials including cortical mandible bone, spongious bone, muscle, CT water, and adipose. The five cylinders are surrounded by CT water. The diameters of phantom is 100 mm and each cylinder is 20 mm. The cortical mandible bone and CT water are used as two basis materials for direct material decomposition. The QRM phantom is scanned twice at tube voltages of 80 and 120 kVp along a circular line. The x-ray tube current is set to 220 μ A for twice scanning. The spectra of the two scans are estimated by a transmission-based method [50] where a cylindrical phantom with uniform known material is scanned under two energy spectra The high- and low-energy projections are sampled at 360° with a scanning interval of 0.5°. The source-to-object and source-to-detector distances is 309.450 and 969.725 mm, respectively. The central slice of each 2D projection is extracted and down-sampled as 1438 bins for the material reconstruction in the experiment. The decomposed images have a dimension of 512×512 with a pixel size of 0.2653 mm × 0.2653 mm. We compare the decomposition results of different methods, and the ROIs that includes the spongious bone on the bone and water basis material maps are magnified to compare the noise suppression and edge preservation. The mean values and STDs of basis materials, i.e., cortical mandible bone and CT water, are calculated on two material maps to quantitatively evaluate the noise level of decomposition results. We further generate the CT images at a tube voltage of 60 keV by linearly forming the decomposed material maps to evaluate the performance of different methods on monochromatic CT image formation.

IV. RESULTS
A. SIMULATION EXPERIMENT
Fig. 5 shows the decomposition results of ESART, TV-based, BM3D-based and proposed methods with L1 and L0 norm from the left to right columns. The tissue and bone material
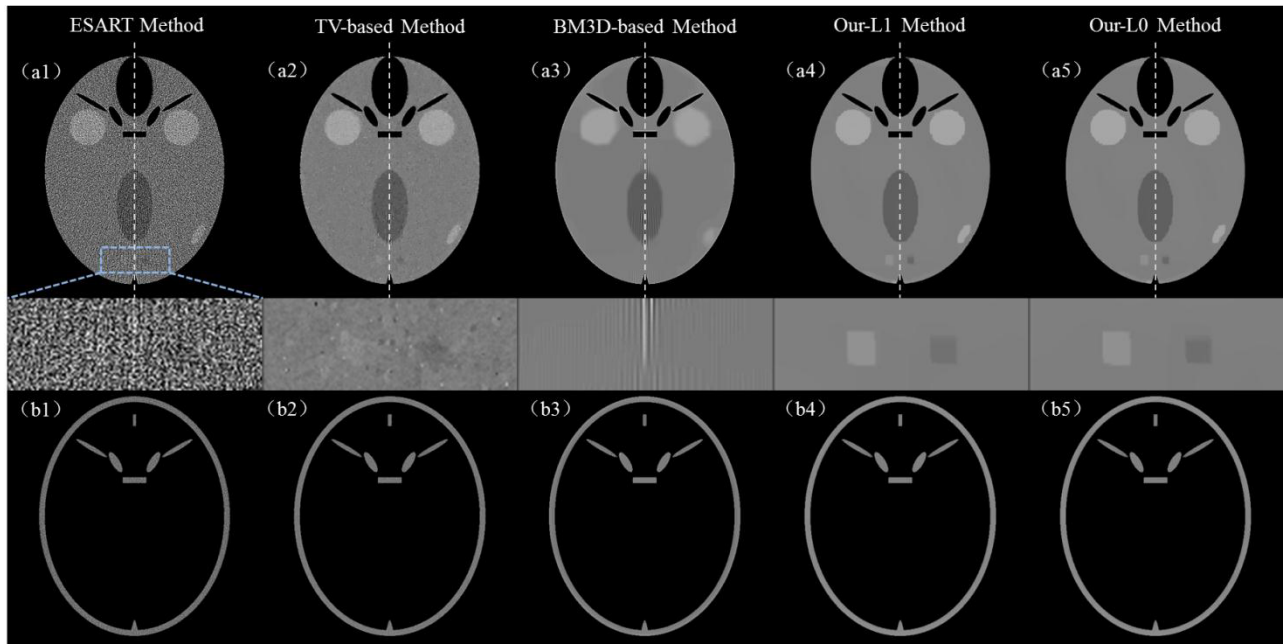
FIGURE 5. Decomposition results of different methods. Left to right columns represent the results of ESART, TV-based, BM3D-based, and the proposed methods with L1 and L0 norm. (a) and (b) represents the tissue and bone material maps, respectively. The blue dashed rectangle denotes the enlarged ROI with low contrast. The display window of all figures is [0.8 1.2].

maps are shown in (a) and (b). An ROI denoted by blue dashed rectangle on the tissue material map (Fig. 5(a1)) is magnified for the comparison of the recoverability of detailed information. This ROI contains two circle areas and they are filled with different materials with low contrast. As shown in Fig. 5 two circle areas in the decomposition results of ESART are flooded by noises and artifacts because the projection noise is magnified during material reconstruction. The TV-based method reduces the decomposition noises to some extent and achieves higher image quality than ESART, but it still fails to recover the two circle areas. The BM3D-based method shows good performance in noise suppression because the reconstruction noises are almost invisible in the material maps. However, the enlarged area of (a3) indicates that it cannot recover the low contrast ROI and the strip false artifacts are introduced into the material map. By contrast, decomposition results of the two proposed methods have better quality. They efficiently suppress the reconstruction noises and remove the false artifacts from the material maps. Although the gray contrast of the enlarged ROI is low, the proposed methods recover them with relatively higher quality than other methods. We also find that the results of the proposed methods with L1 and L0 norm (column 4 and 5) are very close to each other, which indicates that the scheme of the proposed method is insensitive to the form of norms and promising for material reconstruction of DECT.
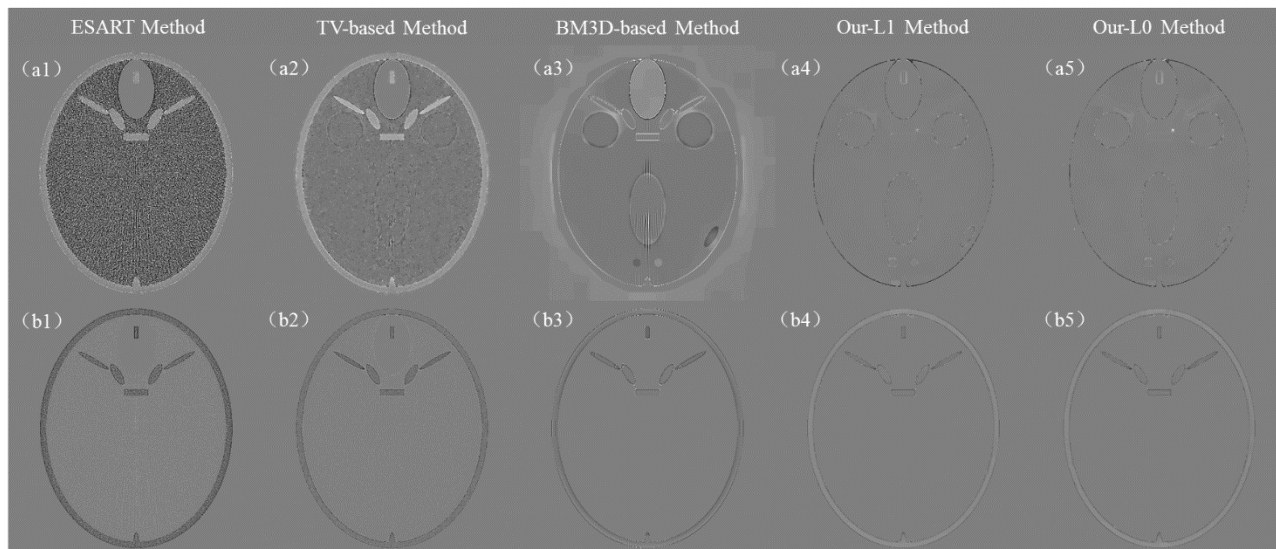
Fig. 6 shows the difference images of decomposition results with the ground truth. ESART is seriously disturbed by noise. The TV-based method reduces the artifacts to some extent, but shows large difference of gray level with the

ground truth for tissue materials. The BM3D-based method contains less noises, but the edge cannot be well preserved. In comparison with the former methods, the proposed methods can efficiently reduce the decomposition noises and obtains better results.
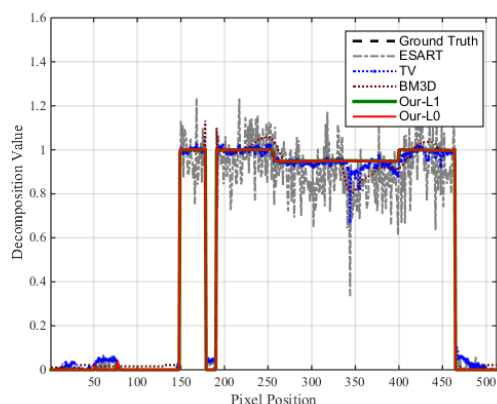
Fig. 7 presents the profiles of decomposition results along the gray dotted line in Fig. 5. The line profile of ESART is sharply fluctuated around the ground truth. The TV-based method is closer to the ground truth than ESART, but it contains many errors on one uniform material and has a large difference with the ground truth in the edge area. The BM3D-based method shows large difference with the ground truth in the adjacent region. The profiles obtained by the proposed methods are the best comparing to the ground truth and generate the steepest profiles in the adjacent region of basis materials, which shows the capability of noise suppression and edge preservation for direct material decomposition.

Table 1 lists the RMSE, SSIM, and PSNR of the decomposed results. We can see that RMSE of the decomposed results by the proposed method is the smallest in both bone and tissue material maps. For example, the proposed method with L0 norm reduces the RMSE by 86.27% and 58.29% on the tissue and bone material maps, respectively, comparing to ESART, while the number is 70.08% and 29.13%, respectively, comparing to the TV-based method. For the metric of SSIM which measures the similarity between maps, the decomposed images of the proposed methods have higher similarity to the ground truths than the results of the other three methods. Regarding to the PSNR, the proposed methods obtain higher values than other methods, which indicates the robustness of the proposed methods.

FIGURE 6. Difference images of decomposition results with the ground truth. Left to right columns represent the results of ESART, TV-based, BM3D-based, and proposed methods with L1 and L0 norm. (a) and (b) represents the tissue and bone material maps, respectively. The display window of all figures is [−0.15 0.15].

FIGURE 7. Line profiles of decomposition results for different methods. Black, gray, blue, crimson, green and red lines denotes the line profiles of the ground truth, ESART, TV-based, BM3D-based, and proposed methods with L1 and L0 norm, respectively.

Table 2 shows the mean and STD values of ROI 1 to 5 indicated in Fig. 2(a) for different methods. The STD values of ROI 1 to 5 are 0 for the ground truth image because they are filled with uniform material, thus only the mean values are listed in Table 2. Regarding the mean values which evaluate the accuracy of the reconstruction method, the mean value of ESART is the largest, which shows the largest difference with the ground truth. The TV-based and BM3D-based methods can reduce the decomposition error and noise STD to some extent, while the proposed method obtains better quantitative results on ROI 1 to 5 than the former methods. More specifically, the proposed method with L0 norm obtains the minimum difference with the ground truth regarding the comparison of mean values. For the noise suppression, the proposed method with L1 norm shows the

best performance because it has the smallest STDs. It reduces the STDs of ROI 1 to 5 by 94.60%, 96.21%, 92.26%, 95.48%, and 96.54% comparing to ESART, while the reductions are 87.52%, 92.32%, 83.81%, 89.22%, and 92.28%, for the TV-based method.

Fig. 8 shows the RMSEs curves of different methods to investigate the convergence. We can find that all the reconstruction methods can converge to a stable solution with a given RMSE. The largest one is obtained by ESART. The TV-based and BM3D-based methods decrease rapidly, but their final values are also unpromising. Compared with the former methods, the RMSE curves of the two proposed methods decrease rapidly and convergent to a smaller RMSE value, which illustrates the convergence of the proposed method. More specifically, the proposed method with L0 norm reaches the minimum RMSE among all compared methods, which is consistent with the evaluation of Table 1 and 2.

Fig. 9 shows the curves of L1 norm of image gradients for different methods. The ground truth of basis materials is known, so the ground truth of the L1 norm of image gradients can be calculated in advance It is 7150.46 and is shown as the red dotted line in Fig. 9. It can be seen that the curves of ESART is far from the ground truth. The TV-based method is very close to the ground truth but it still has a certain distance. The BM3D-method shows strong ability in minimizing the L1 norm of image gradients, but its curve has reached below the truth line. The two proposed methods exhibit better performance than the former methods and both of them converge to the truth value. The comparison of the gradient curves also indicates the convergence of the proposed methods.

Fig. 10 shows the pseudo-monochromatic CT image at 60 keV by linearly forming the material maps in Fig. 5.

TABLE 1. RMSE, SSIM, and PSNR of the decomposed results for different methods.

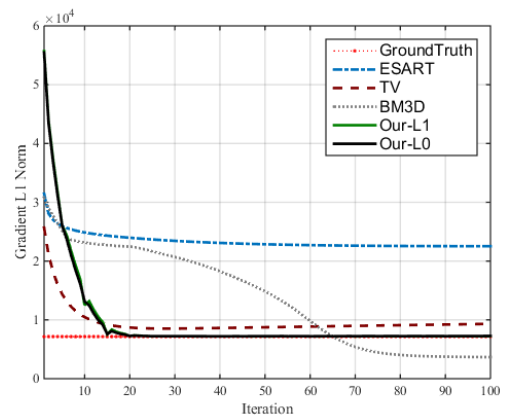| Material	Index	ESART	TV	BM3D	Our-L1	Our-L0
Tissue	RMSE	0.0852	0.0391	0.0209	0.0144	0.0117
	SSIM	0.5519	0.8950	0.8209	0.9947	0.9951
	PSNR	21.3907	34.9628	33.6176	36.8574	38.6291
Bone	RMSE	0.0175	0.0103	0.0118	0.0074	0.0073
	SSIM	0.8998	0.9639	0.9984	0.9994	0.9994
	PSNR	35.1639	39.2247	38.5897	42.5765	42.7783

TABLE 2. Mean and STD values of ROI 1 to 5 in Fig. 2(a) for different methods. For the ground truth, the STD values of these uniform ROIs are 0. Thus, only the mean values are listed.

ROI	Ground truth	ESART	TV	BM3D	Our-L1	Our-L0
1	1.0600	1.0222 ± 0.1185	1.0540 ± 0.0513	1.0491 ± 0.0091	1.0582 ± 0.0064	1.0590 ± 0.0068
2	0.9500	0.9102 ± 0.1240	0.9431 ± 0.0612	0.9478 ± 0.0292	0.9500 ± 0.0047	0.9501 ± 0.0048
3	1.0500	1.0107 ± 0.1163	1.0434 ± 0.0556	1.0224 ± 0.0119	1.0461 ± 0.0090	1.0469 ± 0.0104
4	0.9750	0.9355 ± 0.1106	0.9688 ± 0.0464	0.9937 ± 0.0023	0.9807 ± 0.0050	0.9781 ± 0.0070
5	1.0250	0.9832 ± 0.1243	1.0146 ± 0.0557	0.9959 ± 0.0058	1.0262 ± 0.0043	1.0250 ± 0.0049
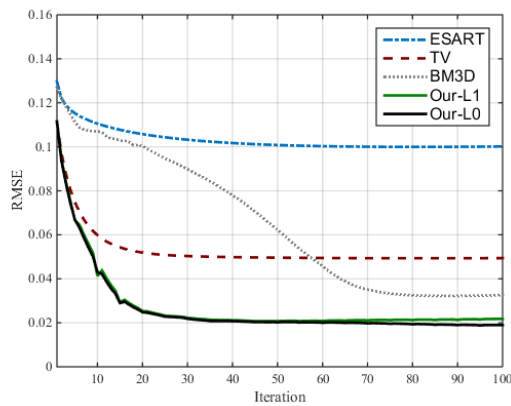
FIGURE 8. RMSEs curves of basis materials for different methods. The blue, crimson, gray, green, and black lines represents the RMSE curve of ESART, TV-based, BM3D-based, and the proposed methods with L1 and L0 norm, respectively.

FIGURE 9. The curves of L1 norm of image gradients for different methods. The red line represents the ground truth. The blue, crimson, gray, green, and black lines represents the curves of ESART, TV-based, BM3D-based, and the proposed methods with L1 and L0 norm, respectively.

We can intuitively find that the pseudo-monochromatic image generated by the proposed methods has lower noise level than those generated by other methods. Thus, we can conclude that the proposed methods can sufficiently suppress decomposition noises while maintaining the material reconstruction accuracy.

B. REAL DATA EXPERIMENT

In the real data experiment, the QRM phantom is scanned at tube voltages of 80 and 120 kVp. Fig. 11 shows the decomposition results of QRM phantom based on the dual-energy measurement projections at tube voltages of 80 and 120 kVp.
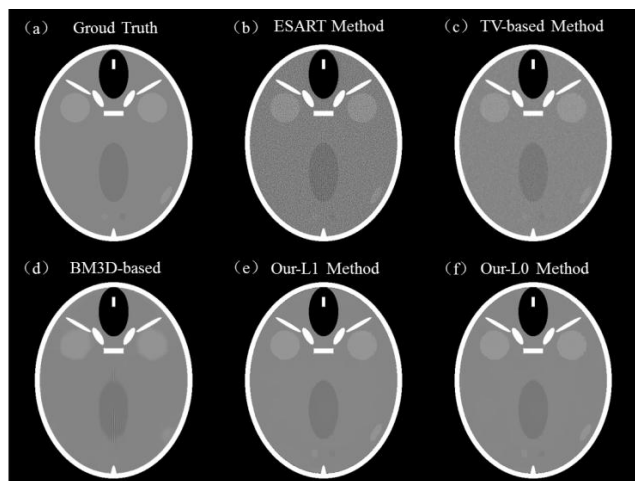
FIGURE 10. Pseudo-monochromatic CT image at 60 keV by linearly forming the material maps in Fig. 5. (a) to (f) represents the results of ground truth, ESART, TV-based, BM3D-based, and proposed methods with L1 and L0 norm, respectively. The display window of all figures is [0.01 0.03].
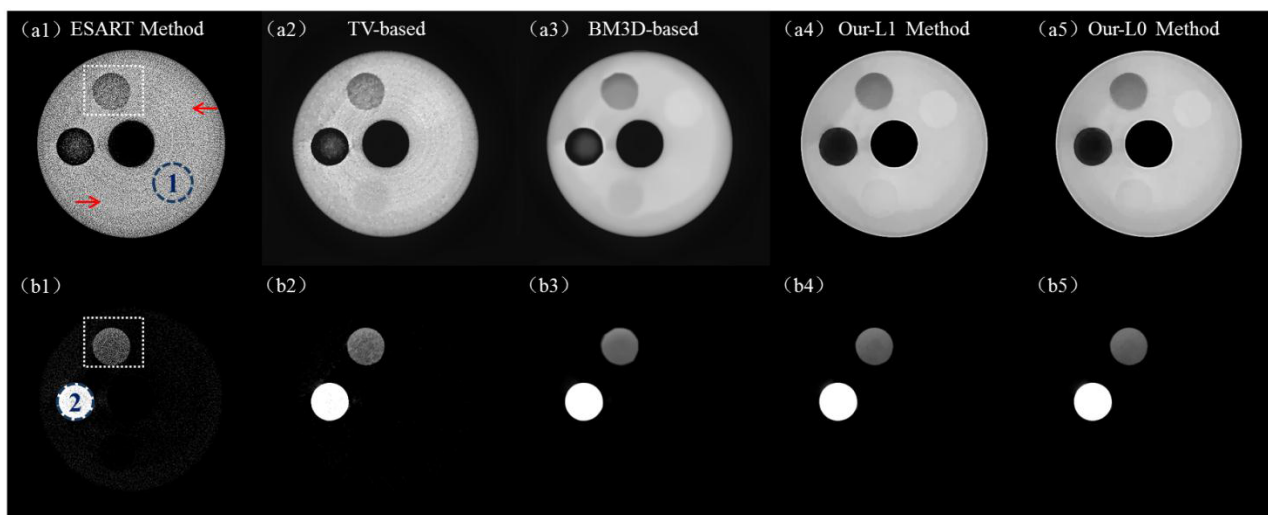
The figures in the columns from left to right represent the decomposition results of ESART, TV-based, BM3D-based, and proposed methods with L1 and L0 norm. The decomposition maps of CT water and cortical mandible bone are represented as (a) and (b), respectively. As shown in Fig. 11, the results of ESART contain serious noises, and the adipose and muscle area indicated by the red arrow are totally flooded by noises. The TV-based method achieves higher image quality than ESART because the adipose and muscle materials on the water material map are relatively more evident than those of ESART. However noises still clearly exist on the water and bone material maps. The BM3D-based method shows strong ability in noise suppression, but it cannot preserve the edges. And again, the two proposed methods can efficiently reduce

the decomposition noises and intuitively provide results with clear edge.

Fig. 12 shows the ROIs of spongious bone indicated by the dotted rectangle in Fig. 11 for further evaluation. We can see that the image noises are seriously magnified on the decomposition results for ESART and TV-based method. The BM3D-based method can efficiently suppress reconstruction noises from the material maps, but it cannot keep the shape of spongious bone. By contrast, the proposed methods show promising performance in noise suppression and both of them recover the image edge with higher accuracy at the same time. We further quantitatively evaluate the noise level of reconstruction results in ROIs 1 and 2 indicated by blue dashed circles in Figs. 11(a1) and (b1).

Table 3 lists the mean values and STDs of ROIs 1 and 2. The results of the proposed method with L1 norm have the smallest STDs for both basis materials among the three methods, which is consistent with the quantitative evaluation of digital phantom in Table 2. In comparison with ESART, the proposed method with L1 norm reduces the STDs on CT water (ROI 1) and cortical mandible bone (ROI 2) by 97.90% and 92.51%, respectively. When it comes to TV-based method, the number reaches 86.08% and 82.29%.

Fig. 13 shows the pseudo-monochromatic CT image of QRM phantom at 60 keV based on the decomposition results in Fig. 11. The pseudo-monochromatic CT images provided by the two proposed methods have higher quality than the results of other three methods. The ROIs of spongious bone and adipose on the pseudo-monochromatic CT images are selected for the comparison of zoom-in view. In the zoom-in view of ROI 1, the results of ESART and TV-based method are seriously disturbed by decomposition noises, and the BM3D method shows worse performance in edge preservation. For the ROI 2, the adipose edge is seriously degraded because it looks blurred for the ESART, TV-based,
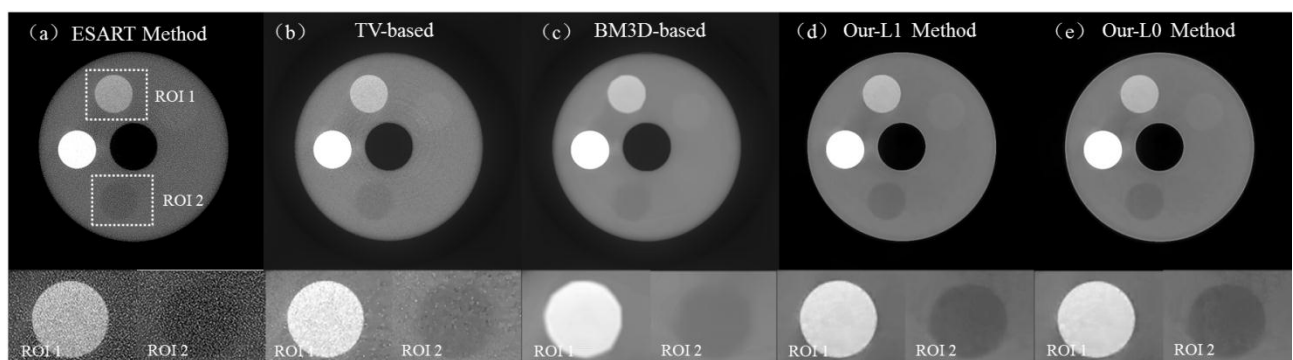

FIGURE 11. Decomposition results of QRM phantom for different methods. Left to right columns represent the results of ESART, TV-based, BM3D-based, and proposed methods with L1 and L0 norm. (a) and (b) denotes the material maps of the cortical mandible bone and CT water, respectively. The display windows of (a) and (b) is [0 1.2] and [0.15 0.8], respectively.
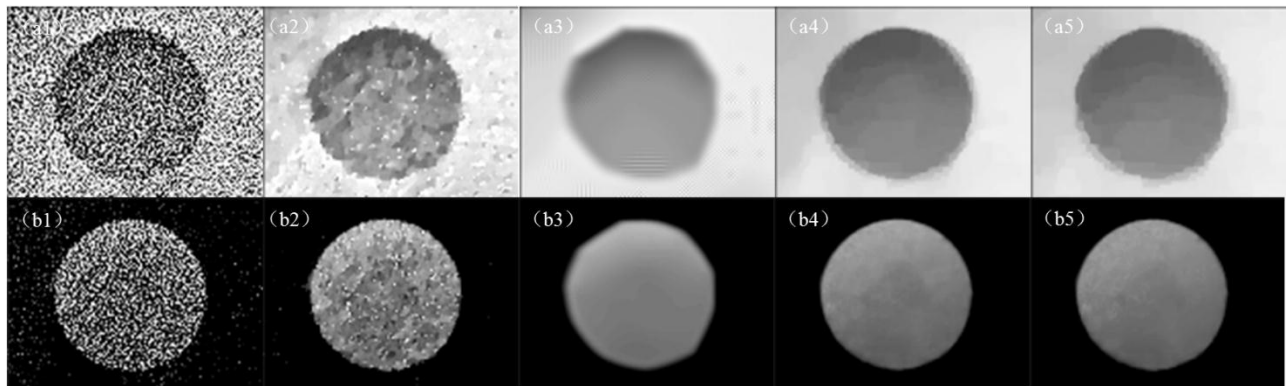
FIGURE 12. Enlarged ROIs of decomposition results indicated by dotted rectangle in Fig. 11. Left to right columns represent the results of ESART, TV-based, BM3D-based, and proposed methods with L1 and L0 norm. (a) and (b) denotes the material maps of the cortical mandible bone and CT water, respectively. The display windows of (a) and (b) is [0.2 1.0] and [0.2 0.6], respectively.

TABLE 3. Mean and STD values of ROIs 1 and 2 indicated in Fig. 11(A1) and (B1) for different methods.

ROI	ESART	TV	BM3D	Our-L1	Our-L0
1	0.8576 ± 0.3909	0.9447 ± 0.0589	0.9431 ± 0.0266	0.9440 ± 0.0082	0.9436 ± 0.0088
2	0.9435 ± 0.2150	1.0497 ± 0.0909	1.0482 ± 0.0488	1.0443 ± 0.0161	1.0441 ± 0.0174

FIGURE 13. Pseudo-monochromatic CT images of QRM phantom at 60 keV by linearly forming the material maps in Fig. 11. Left to right columns represents the results of ESART, TV-based, BM3D-based, and proposed methods with L1 and L0 norm, respectively. ROIs 1 and 2 indicated by dashed rectangle are enlarged for detailed comparison. The display window of pseudo-monochromatic CT images is [0 0.05]. The display window of enlarged views is [0.01 0.04].

and BM3D-based methods. However, both noise suppression and edge preservation can achieve better performance in the proposed methods. The ROIs of spongious bone and adipose are recovered with high quality, especially for the ROI 2 of adipose. Therefore, the evaluation of pseudo-monochromatic CT image again indicates that the proposed methods show better performance in direct material reconstruction.

V. DISCUSSIONS AND CONCLUSIONS

We proposed a one-step method for the material reconstruction of DECT to reduce the amplified noises resulting from high- and low-energy projection data. A new reconstruction model was established by incorporating TV and BM3D frame. TV regularization term preserves the sparsity in the gradient domain of material maps and help to maintain the image edge. BM3D frame aims to depict the

similarities of image patches combined with sparse transform. Alternating direction method was applied to solve the optimization problems by splitting them into three subproblems. For block matching-based denoising, we designed a new denoising strategy by introducing the reconstructed polychromatic CT images as the prior image to generate the pilot signal for the block grouping in the following step.

For direct reconstruction methods of DECT, it is necessary for the final decomposition results to accurately estimate the high- and low-energy x-ray spectra. The estimation errors of x-ray energy spectrum will compromise the accuracy of the final decomposed material maps. In the experiments on real data, image artifacts and quantitative errors caused by the estimation error appear in the final results and thus more accurate estimation methods are needed. But the comparison of these direct reconstruction methods is fair because

the same estimated x-ray spectrum is used to evaluate their performance in direct material reconstruction. For the image denoising, the low-energy CT image is used to generate the pilot image for the final estimates. However, if the high-energy CT image had lower noise level and higher image quality than the low-energy CT image at a certain scanning setting, it is also feasible to use the high-energy CT image to generate the basic estimate. For the enlarged ROI of the digital and real data results (Figs. 5 and 10), edge distortions can be still observed in the decomposition results although the proposed method has shown better performance in edge preservation than the compared methods. This problem will be solved by incorporating the weights of TV regularization terms, wherein the edge weights of intermediate reconstruction are incorporated into the TV objective function. The proposed method solves the new direct reconstruction model based on the frame of ADM, it is also a meaningful work to apply different algorithms to solve the non-convex optimization problem, such as fast iterative shrinkage-thresholding algorithm, Bregman iterative algorithm, and proximal point method.

For the iteration method of CT imaging, forward and back forward projection are performed in each iteration, which is timeconsuming. To accelerate the implementation, we program forward and back forward projection at the platform of C++ by encapsulating them as a mexw64 file for Matlab and use graphic processing unit (GPU). In this way, the running time of forward and back forward projection can be largely reduced to approximately 0.01–0.03 s for the digital phantom experiment, where each reconstruction image is 512×512 and the length of detector is 1024. Furthermore, since the solution of the non-convex problem can be obtained by solving three sub-problems each of the sub-problems has some tricks to be solved The first sub-problem can be directly solved by the shrinkage operator. The second sub-problem utilizes the fast Fourier transform to calculate the pseudo-inverse term, which highly reduce the computational expensive. The running time to compute the first and second sub-problem is about 0.4–0.5 s. For the solution of the third sub-problem, block matching is computationally demanding due to the searching of similar patches. On the basis of [48], GPU is also applied in our work to accelerate the implementation of BM3D-based denoising. The running time of per round of block matching denoising is approximately 0.9–1.2 s for a image with 512×512 pixels. Overall, the total time of each iteration is approximately 1.45 s for the proposed method in our environment.

In conclusion, we proposed an efficient one-step method based on TV and block matching regularization for direct material reconstruction from dual-energy projections. The experiments on digital phantom and real data verified the capability of the proposed method in direct material reconstruction and demonstrated that the proposed method outperformed its counterparts. The proposed method can be further modified by changing the regularization terms such as total p-variation, wavelet tight frame, and

Kullback–Leibler divergence, according to different imaging tasks. The proposed method can also be further applied into the area of low-dose CT reconstruction, incomplete data CT reconstruction, and photon counting CT reconstruction

APPENDIX

The initial problem of Eq. (1) can be written as

$$\mathbf{p}_j(\mathbf{b}_1, \mathbf{b}_2)$$
$$= \mathbf{p}_j^k + \frac{\mathbf{O}_j^k}{\mathbf{q}_j^k} \mathcal{A}\left(\mathbf{b}_1 - \mathbf{b}_1^k\right) + \frac{\Theta_j^k}{\mathbf{q}_j^k} \mathcal{A}\left(\mathbf{b}_2 - \mathbf{b}_2^k\right), \quad j = H, L,$$
(27)

where

$$\mathbf{q}_j^k = \sum_m S_{j_m} \exp\left(-\mu_{1m} A \mathbf{b}_1^k - \mu_{2m} A \mathbf{b}_2^k\right),$$

$$\mathbf{p}_j^k = -\ln \sum_m S_{j_m} \exp\left(-\mu_{1m} A \mathbf{b}_1^k - \mu_{2m} A \mathbf{b}_2^k\right),$$

$$\mathbf{O}_j^k = \sum_m S_{j_m} \mu_{1m} \exp\left(-\mu_{1m} A \mathbf{b}_1^k - \mu_{2m} A \mathbf{b}_2^k\right),$$

$$\Theta_j^k = \sum_m S_{j_m} \mu_{2m} \exp\left(-\mu_{1m} A \mathbf{b}_1^k - \mu_{2m} A \mathbf{b}_2^k\right). \quad (28)$$

Let $\tilde{P}_i^k$ represent the projection difference of the *i*th basis material with the ground truth. Then, the linearization of the data model can be written as

$$\mathbf{p}_j(\mathbf{b}_1, \mathbf{b}_2) = \mathbf{p}_j^k + \frac{\mathbf{O}_j^k}{\mathbf{q}_j^k} \tilde{\mathcal{P}}_1^k + \frac{\Theta_j^k}{\mathbf{q}_j^k} \tilde{\mathcal{P}}_2^k, j = H, L. \quad (29)$$

$\tilde{\mathcal{P}}_i^k$ can be obtained by solving the above model using the projection method [51]:

$$\begin{cases} \tilde{\mathcal{P}}_{1j}^k = \dfrac{\mathbf{O}_j^k \mathbf{q}_j^k}{\left(\mathbf{O}_j^k\right)^2 + \left(\Theta_j^k\right)^2} \left(\mathbf{p}_j - \mathbf{p}_j^k\right) \\[4mm] \tilde{\mathcal{P}}_{2j}^k = \dfrac{\Theta_j^k \mathbf{q}_j^k}{\left(\mathbf{O}_j^k\right)^2 + \left(\Theta_j^k\right)^2} \left(\mathbf{p}_j - \mathbf{p}_j^k\right). \end{cases} \quad (30)$$

Thus, we obtain the approximated expression of the projection difference of $\mathbf{b}_1$ and $\mathbf{b}_2$ at the basis of linear operator A

REFERENCES

[1] A. N. Primak, J. G. Fletcher, T. J. Vrtiska, O. P. Dzyubak, J. C. Lieske, M. E. Jackson, J. C. Williams, Jr., and C. H. McCollough, "Noninvasive differentiation of uric acid versus non-uric acid kidney stones using dual-energy CT," *Academic Radiol.*, vol. 14, no. 12, pp. 1441–1447, 2007.

[2] C. H. McCollough, S. Leng, L. Yu, and J. G. Fletcher, "Dual- and multi-energy CT: Principles, technical approaches, and clinical applications," *Radiology*, vol. 276, no. 3, pp. 637–653, 2015.

[3] M. Li, Y. Zhao, and P. Zhang, "Accurate iterative FBP reconstruction method for material decomposition of dual energy CT," *IEEE Trans. Med. Imag.*, vol. 38, no. 3, pp. 802–812, Mar. 2019.

[4] R. E. Alvarez and A. Macovski, "Energy-selective reconstructions in X-ray computerised tomography," *Phys. Med. Biol.*, vol. 21, no. 5, pp. 733–744, 1976.

[5] W. A. Kalender, W. H. Perman, J. R. Vetter, and E. Klotz, "Evaluation of a prototype dual-energy computed tomographic apparatus. I. Phantom studies," *Med. Phys.*, vol. 13, no. 3, pp. 334–339, 1986.

[6] M. Daniele, T. B. Daniel, M. Achille, and C. N. Rendon, "State of the Art: Dual-energy CT of the abdomen," *Radiology*, vol. 271, no. 2, pp. 327–342, 2014.

[7] A. Graser, T. Johnson, M. Bader, M. Staehler, N. Haseke, K. Nikolaou, M. Reiser, C. Stief, and C. Becker, "Dual energy CT characterization of urinary calculi: Initial *in vitro* and clinical experience," *Investigative Radiol.*, vol. 43, no. 2, pp. 112–119, 2008.

[8] H. Voit, B. Krauss, M. C. Heinrich, A. Dimmler, B. Adamitz, F. M. Hinkmann, M. Uder, and A. Kuettner, "Dual-source-CT: *in-vitro*-Charakterisierung von Gallensteinen mittels dual-energy-Analyse," *RöFo-Fortschritte Auf Dem Gebiet der Röntgenstrahlen und der Bildgebenden Verfahren*, vol. 181, no. 4, pp. 367–373, 2009.

[9] Y. Xue, R. Ruan, X. Hu, Y. Kuang, J. Wang, Y. Long, and T. Niu, "Statistical image-domain multimaterial decomposition for dual-energy CT," *Med. Phys.*, vol. 44, no. 3, pp. 886–901, 2017.

[10] E. Roessl and R. Proksa, "K-edge imaging in X-ray computed tomography using multi-bin photon counting detectors," *Phys. Med. Biol.*, vol. 52, no. 15, pp. 4679–4696, 2007.

[11] D. S. Rigie and P. J. La Rivière, "Joint reconstruction of multi-channel, spectral CT data via constrained total nuclear variation minimization," *Phys. Med. Biol.*, vol. 60, no. 5, pp. 1741–1762, 2015.

[12] H. Turbell, "Cone-beam reconstruction using filtered backprojection," Ph.D. dissertation, Dept. Elect. Eng., Linköping Univ., Linköping, Sweden, 2001.

[13] M. Petersilka, H. Bruder, B. Krauss, K. Stierstorfer, and T. G. Flohr, "Technical principles of dual source CT," *Eur. J. Radiol.*, vol. 68, no. 3, pp. 362–368, 2008.

[14] J. Hsieh, "TU-E-210A-01: Dual-energy CT with fast-KVp switch," *Med. Phys.*, vol. 36, no. 6, p. 2749, 2009.

[15] T. Niu, X. Dong, M. Petrongolo, and L. Zhu, "Iterative image-domain decomposition for dual-energy CT," *Med. Phys.*, vol. 41, no. 4, 2014, Art. no. 041901.

[16] J. Harms, T. Wang, M. Petrongolo, T. Niu, and L. Zhu, "Noise suppression for dual-energy CT via penalized weighted least-square optimization with similarity-based regularization," *Med. Phys.*, vol. 43, no. 5, pp. 2676–2686, 2016.

[17] B. Chen, Z. Zhang, E. Y. Sidky, D. Xia, and X. Pan, "Image reconstruction and scan configurations enabled by optimization-based algorithms in multispectral CT," *Phys. Med. Biol.*, vol. 62, no. 22, pp. 8763–8793, 2017.

[18] Y. Long and J. A. Fessler, "Multi-material decomposition using statistical image reconstruction for spectral CT," *IEEE Trans. Med. Imag.*, vol. 33, no. 8, pp. 1614–1626, Aug. 2014.

[19] W. Wu, Q. Wang, F. Liu, Y. Zhu, and H. Yu, "Block matching frame based material reconstruction for spectral CT," 2018, *arXiv:1810.10346*. [Online]. Available: https://arxiv.org/abs/1810.10346

[20] J. Liu, H. Ding, S. Molloi, X. Zhang, and H. Gao, "TICMR: Total image constrained material reconstruction via nonlocal total variation regularization for spectral CT," *IEEE Trans. Med. Imag.*, vol. 35, no. 12, pp. 2578–2586, Dec. 2016.

[21] E. Y. Sidky and X. Pan, "Image reconstruction in circular cone-beam computed tomography by constrained, total-variation minimization," *Phys. Med. Biol.*, vol. 53, no. 17, pp. 4777–4807, 2008.

[22] Z. Chen, X. Jin, L. Li, and G. Wang, "A limited-angle CT reconstruction method based on anisotropic TV minimization," *Phys. Med. Biol.*, vol. 58, no. 7, pp. 2119–2141, 2013.

[23] H.-M. Zhang, L.-Y. Wang, B. Yan, L. Li, X.-Q. Xi, and L.-Z. Lu, "Image reconstruction based on total-variation minimization and alternating direction method in linear scan computed tomography," *Chin. Phys. B*, vol. 22, no. 7, 2013, Art. no. 078701.

[24] B. Shi, S. Chen, Y. Tian, X. Fan, and Q. Lian, "FASPR: A fast sparse phase retrieval algorithm via the epigraph concept," *Digit. Signal Process.*, vol. 80, no. 9, pp. 12–26, Sep. 2018.

[25] R. F. Barber, E. Y. Sidky, T. G. Schmidt, and X. Pan, "An algorithm for constrained one-step inversion of spectral CT data," *Phys. Med. Biol.*, vol. 61, no. 10, pp. 3784–3818, 2016.

[26] B. Chen, Z. Zhang, D. Xia, E. Y. Sidky, and X. Pan, "Algorithm-enabled partial-angular-scan configurations for dual-energy CT," *Med. phys.*, vol. 45, no. 5, pp. 1857–1870, 2018.

[27] J. Bian, J. H. Siewerdsen, X. Han, E. Y. Sidky, J. L. Prince, C. A. Pelizzari, and X. Pan, "Evaluation of sparse-view reconstruction from flat-panel-detector cone-beam CT," *Phys. Med. Biol.*, vol. 55, no. 22, pp. 6575–6599, 2010.

[28] J. Tang, B. E. Nett, and G. H. Chen, "Performance comparison between total variation (TV)-based compressed sensing and statistical iterative reconstruction algorithms," *Phys. Med. Biol.*, vol. 54, no. 19, pp. 5781–5804, 2009.

[29] S. Niu, G. Yu, J. Ma, and J. Wang, "Nonlocal low-rank and sparse matrix decomposition for spectral CT reconstruction," *Inverse Problems*, vol. 34, no. 2, 2018, Art. no. 024003.

[30] W. Wu, F. Liu, Y. Zhang, Q. Wang, and H. Yu, "Non-local low-rank cube-based tensor factorization for spectral CT reconstruction," 2018, *arXiv:1807.10610*. [Online]. Available: https://arxiv.org/abs/1807.10610

[31] J. Chu, L. Li, Z. Chen, G. Wang, and H. Gao, "Multi-energy CT reconstruction based on low rank and sparsity with the split-Bregman method (MLRSS)," in *Proc. IEEE Nucl. Sci. Symp. Med. Imag. Conf. Rec. (NSS/MIC)*, Anaheim, CA, USA, Oct. /Nov. 2012, pp. 2411–2414.

[32] K. Kim, J. C. Ye, W. Worstell, J. Ouyang, Y. Rakvongthai, G. El Fakhri, and Q. Li, "Sparse-view spectral CT reconstruction using spectral patch-based low-rank penalty," *IEEE Trans. Med. Imag.*, vol. 34, no. 3, pp. 748–760, Mar. 2015.

[33] Y. Zhang, X. Mou, G. Wang, and H. Yu, "Tensor-based dictionary learning for spectral CT reconstruction," *IEEE Trans. Med. Imag.*, vol. 36, no. 1, pp. 142–154, Jan. 2016.

[34] W. Wu, Y. Zhang, Q. Wang, F. Liu, P. Chen, and H. Yu, "Low-dose spectral CT reconstruction using image gradient ℓ_0-norm and tensor dictionary," *Appl. Math. Model.*, vol. 63, pp. 538–557, Nov. 2018.

[35] D. Zeng, J. Huang, H. Zhang, "Spectral CT image restoration via an average image-induced nonlocal means filter," *IEEE Trans. Biomed. Eng.*, vol. 63, no. 5, pp. 1044–1057, May 2016.

[36] Q. Xu, H. Yu, X. Mou, L. Zhang, J. Hsieh, and G. Wang, "Low-dose X-ray CT reconstruction via dictionary learning," *IEEE Trans. Med. Imaging*, vol. 31, no. 9, pp. 1682–1697, Sep. 2012.

[37] A. Cai, L. Li, Z. Zheng, H. Zhang, L. Wang, G. Hu, and B. Yan, "Block matching sparsity regularization-based image reconstruction for incomplete projection data in computed tomography," *Phys. Med. Biol.*, vol. 63, no. 3, 2018, Art. no. 035045.

[38] K. Dabov, A. Foi, V. Katkovnik, and K. Egiazarian, "Image denoising by sparse 3-D transform-domain collaborative filtering," *IEEE Trans. Image Process.*, vol. 16, no. 8, pp. 2080–2095, Aug. 2007.

[39] A. Danielyan, V. Katkovnik, and K. Egiazarian, "BM3D frames and variational image deblurring," *IEEE Trans. Image Process.*, vol. 21, no. 4, pp. 1715–1728, Apr. 2012.

[40] A. P. Harrison, Z. Xu, A. Pourmorteza, D. A. Bluemke, and D. J. Mollura, "A multichannel block-matching denoising algorithm for spectral photon-counting CT images," *Med. Phys.*, vol. 44, no. 6, pp. 2447–2452, 2017.

[41] S. Morteza, Y. Zhang, and H. Yu, "Iterative spectral CT reconstruction based on low rank and average-image-incorporated BM3D," *Phys. Med. Biol.*, vol. 63, no. 15, 2018, Art. no. 155021.

[42] B. Shi, Q. Lian, X. Huang, and N. An, "Constrained phase retrieval: When alternating projection meets regularization," *J. Opt. Soc. Amer. B*, vol. 35, no. 6, pp. 1271–1281, 2018.

[43] B. Shi, Q. Lian, and X. Fan, "PPR: Plug-and-play regularization model for solving nonlinear imaging inverse problems," *Signal Process.*, vol. 162, no. 9, pp. 83–96, 2019.

[44] Y. Zhao, X. Zhao, and P. Zhang, "An extended algebraic reconstruction technique (E-ART) for dual spectral CT," *IEEE Trans. Med. Imag.*, vol. 34, no. 3, pp. 761–768, Mar. 2015.

[45] L. Li, "Research on image reconstruction algorithms of dual energy computed tomography," Ph. D. dissertation, Dept. Inf. Syst. Eng., Inf. Eng. Univ., Zhengzhou, China, 2016.

[46] Y. Xiao and H.-N. Song, "An inexact alternating directions algorithm for constrained total variation regularized compressive sensing problems," *J. Math. Imag. Vis.*, vol. 44, no. 2, pp. 114–127, 2012.

[47] M. K. Ng and R. J. Plemmons, "Fast recursive least squares adaptive filtering by fast Fourier transform-based conjugate gradient iterations," *SIAM J. Sci. Comput.*, vol. 17, no. 4, pp. 920–941, 1996.

[48] D. Honzátko and M. Kruliš, "Accelerating block-matching and 3D filtering method for image denoising on GPUs," in *J. Real-Time Image Processing*. Berlin, Germany: Springer, 2017, pp. 1–15.

[49] J. Hu, X. Zhao, and F. Wang, "An extended simultaneous algebraic reconstruction technique (E-SART) for X-ray dual spectral computed tomography," *Scanning*, vol. 38, no. 6, pp. 599–611, 2016.

[50] L. Li, L. Wang, X. Xi, Y. Han, B. Yan, and S. Bao, "X-ray CT energy spectrum estimation algorithm based on weighted TV normalization," *Spectrosc. Spectral Anal.*, vol. 37, no. 7, pp. 2230–2236, 2017.

[51] K. Tanabe, "Projection method for solving a singular system of linear equations and its applications," *Numerische Mathematik*, vol. 17, no. 3, pp. 203–214, 1971.